Effects of lateral resistances in photovoltaic cells and full 2-D parameter extraction for the spatially-resolved models using electroluminescence images

Effects of lateral resistances in photovoltaic cells and full 2-D parameter extraction for the spatially-resolved models using electroluminescence images

Xiaofeng Wu*, Martin Bliss, Thomas R. Betts and Ralph Gottschalg

Centre for Renewable Energy Systems Technology (CREST), Loughborough University, Loughborough, LE11 3TU
*Corresponding author: x.wu2@lboro.ac.uk, +44 (0)1509 635373

Abstract

This paper investigates the influences of the lateral resistances in photovoltaic (PV) devices, and proposes a method for extracting local electrical parameters of thin-film PV devices based on a 2-D spatially-resolved model utilising electroluminescence (EL) images and 2-D fittings. PV-oriented nodal analysis (PVONA) is used for studying the electrical properties of the devices and for simulations in iterative 2-D fitting processes. It is shown that the effects of the lateral resistances should not be simply replaced by lumped effective resistances. The proposed new method employs firstly the dark-I-V fitting for the junction parameters; and secondly 2-D fitting of EL images taken under varying bias levels, for the internal and lateral series resistances. The method is verified by a case study and demonstrates excellent agreements with measurement data.

1. Introduction

A photovoltaic (PV) cell is commonly considered as a flat diode with a large area. Hence the conventional lumped modelling and characterisation techniques are insufficient to describe the performance of PV devices, especially in the presence of inhomogeneities. Advanced modelling and characterisation techniques have been developed to detect and describe inhomogeneities in PV cells in a spatially-resolved manner, i.e. considering the spatial variations in the devices.

Common spatially-resolved characterisation techniques can be categorised into scanning e.g. light/laser beam induced current (LBIC) [1] and imaging e.g. electroluminescence (EL) [2], photoluminescence (PL) [3] and lock-in thermography (LIT) [4]. Luminescence imaging techniques are considered to be more efficient than scanning techniques and thermography due to the shorter operation time and the easier and more cost-effective setup. However, the qualitative nature limits them to fully reconstruct the behaviour of the devices tested.

Studies on imaging techniques for quantitative interpretation have been reported in recent years. For example, Hinken *et al*. [5] proposed a method that uses differential EL images with respect to the applied voltage to yield the effective series resistance map. The method given by Kampwerth *et al*. [6] utilised an EL image and a PL image obtained under two different operating points but with the same luminescence intensities to map the effective series resistances. Breitenstein *et al*. [7] introduced iterative algorithms to fit the local series resistances and the dark saturation current from EL images take at two biases. Shen *et al*. [8] developed a PL-based parameter extraction method that utilizes at least 5 PL images taken under different conditions to derive an abundant set of localised parameters of the double-diode model.

However, none of these approaches can provide full parameter sets for the 2-D model as presented in [9, 10]. One of the major differences is that these methods use the "effective series resistance" (R_S^*) to represent the localised resistive effects in the devices, in which the internal (e.g. the resistance in the junction) and the external (e.g. the lateral resistance in the contact schemes) resistances are mixed. The use of R_S^* simplifies the theoretical analyses for building up links between a 2-D model and measurement results i.e. images. However, the validity of using R_S^* in 2-D modelling has not been fully proven.

In this paper, the effects of the lateral resistances and the validity of the R_S^* are investigated through 2-D modelling and simulations. A new iterative method for extracting the full parameter set of the 2-D spatially-resolved model (SRM) for thin-film PV devices is presented with a case study.

2. Effects of lateral resistances

The variations of the lateral resistance ($R_{\blacksquare}$) are large for different types of PV materials. For example, the $R_{\blacksquare}$ for the transparent conducting oxide (TCO) layer of a thin-film device is normally in the range 5-20Ω/□, while for the emitter layer of a c-Si device, it can be around 80-100Ω/□. To investigate the effects of varying $R_{\blacksquare}$ on these two types of PV devices, PVONA-based simulations are setup to simulate a c-Si cell with 3 fingers and a thin-film 3-cell module.

The varying $R_{\blacksquare}$ values demonstrate immediate impacts on the overall I-V characteristics in Fig. 1(a) and Fig. 2(a) by resulting in different global series resistance (R_s) effects i.e. the variations in the knee areas. The voltage and current maps reveal the lateral variations in the cells. For better demonstration, line-plots along the width of the devices are used. The cells are configured to operate at specified testing voltages (V_{test}) as marked on the I-V curves.

For the c-Si cell, in Fig. 1(b) and Fig. 1(c), the voltage profile clearly show that, unsurprisingly, the largest $R_{\blacksquare}$ (120Ω/□) produces the highest peak voltages, and thus the most distinct lateral variations i.e. voltage drops in the areas between the fingers. This is due to the fact that a higher $R_{\blacksquare}$ can result in greater lateral voltage drops so that the voltage across the metal grid retains V_{test}. Correspondingly, a higher local voltage results in a lower operating current, according to the local I-V characteristics.

Compared to c-Si devices, thin-film products are more sensitive to lateral resistive losses because the current needs to flow through the full width of the cell (normally around 1cm width), while the distance between two fingers in a c-Si cell is normally only a few millimetres. The line-plots across the width of the modules (3 cells) are shown in Fig. 2(b) and Fig. 2(c) clearly reveal the patterns of the voltage drops due to the increasing $R_{\blacksquare}$ and the corresponding changes of the local current distributions. A gradient is evident in both voltage and current profiles. This also explains the reason why the EL images of thin-film devices always show the gradient along the width of each cell.

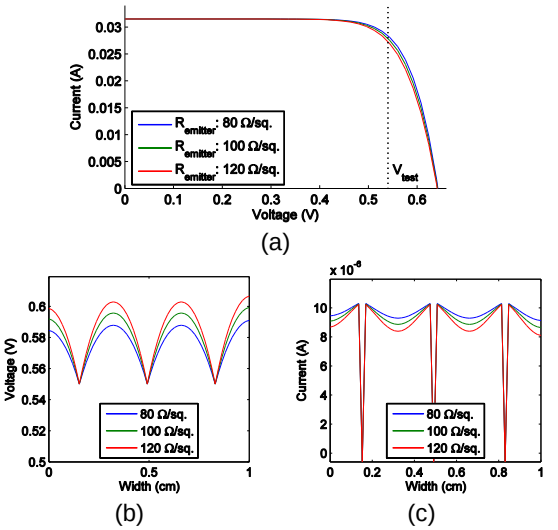

Fig. 1. (a). Simulated I-V curves of the 3 virtual c-Si cells with varying $R_{\blacksquare}$ values; (b) and (c). Line-plots show the voltage and current profiles of the 3 cells operating at V_{test}.

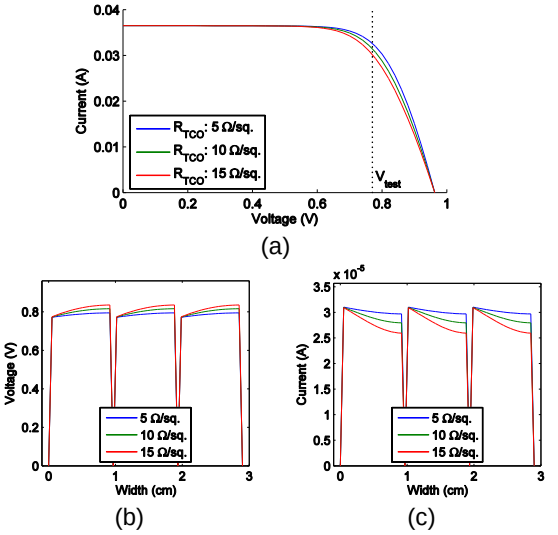

Fig. 2. (a). Simulated I-V curves of the 3 3-cell thin-film modules with varying $R_{\blacksquare}$ values; (b) and (c). Line-plots show the voltage and current profiles of the 3 modules operating at V_{test}.

3. Effective series resistance

The consideration of $R_{\blacksquare}$ distinguishes the SRMs. The utilisation of the resistor networks for the front and back contact schemes builds up connections between the sub-cells through the lateral current flows and lateral voltage drops. But at the same time, it complicates the characterisation by introducing a variable $R_{\blacksquare}$ which is implicit and is coupled with respect to the global resistive effects. Monokroussos *et al*. [11] proposed an initial study on the influences of the $R_{\blacksquare}$ with respect to the width of cells using a 1-D distributed model.

To date, there have been a number of EL-based R_s extraction methods published. Many of them are based on the effective series resistance (R_s^*), as illustrated in Fig. 3. Specifically, for a location $\boldsymbol{r}$ = (x, y), the local R_s^* is defined by

$$R_s^*(\boldsymbol{r}) = \frac{V_{term} - V_j(\boldsymbol{r})}{I(\boldsymbol{r})} \quad (1)$$

where V_{term} is the terminal voltage; $V_j(\boldsymbol{r})$ is the local junction voltage and $I(\boldsymbol{r})$ is the local operating current. The R_s^* includes the effects of both the internal (vertical) R_s^i in the bulk of the cell and the lateral $R_{\blacksquare}$ in the contact schemes.

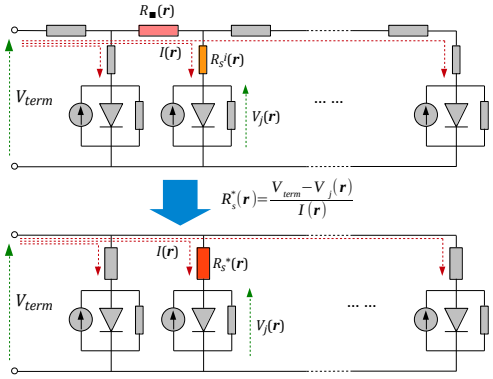

Fig. 3. 1-D model shows the definition of the local effective series resistances.

However, this simplification can introduce uncertainties and thus misinterpretation of the local R_s effects, especially when there are local defects e.g. shunts. Fig. 4 shows simulated junction voltage maps (V_{term} = 1.0V) and the changes of local R_s^* with respect to V_{term} of a thin-film cell with a 60×15 SRM. It suggests that R_s^* is nonlinear and voltage-dependent, although it shows linearity at the lower voltage range. When a local shunt is introduced e.g. at location (30, 7), the nonlinearity effect becomes more significant. Moreover, the linearity remains in the lower voltage range, but the calculated results of effective series resistance do not show a match with those obtained in the non-shunted case.

This is mainly because $V_j(\boldsymbol{r})$ and $I(\boldsymbol{r})$ in Eqn. (1) hold a nonlinear relationship, i.e. the diode equation, where the conductivity of the diode increases exponentially along with the local voltage. The local shunt becomes a current sink and extracts current from the surrounding area [Fig. 4(c)] through $R_{\blacksquare}$. This implicitly changes the local operating points in the affected area and therefore brings severer uncertainties. These mean that the use of the R_s^* can result in misinterpretation of 2-D behaviour of PV cells.

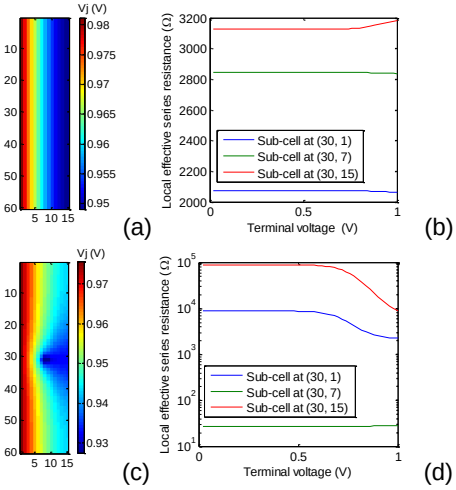

Fig. 4. (a) and (c). V_j maps of the SRM under EL with I_{SC} bias; (b) and (d). Calculated local R_s^* with respect to changing V_{term} of 3 sub-cells.

4. Parameter extraction considering lateral resistances

To extract to full parameter set with separated $R_{\blacksquare}$, the method proposed here requires a sample without visible defects, which can be confirmed by EL measurements. The measurements involved are dark I-V and EL under different forward current bias levels. The algorithm firstly utilises a hybrid fitting method [12] to extract parameters I_{sat}, n and R_{sh} from the dark I-V curve, and secondly searches the optimum R_s^i-$R_{\blacksquare}$ pair that generates the minimum relative mean-square deviation (RMSD) [13] between the simulated and measured EL images under various bias condition, as well as the dark I-V curve simultaneously. It is notable that the method is invalid to be directly applied to a shunted device because the electrical mismatch effects may significantly reshape the I-V characteristics and thus the global parameters extracted by the hybrid fitting algorithm can become a coarse approximation of the overall performance. The dark I-V is chosen to eliminate the possible effects of nonlinear I_{ph} in e.g. a-Si devices, as discussed in [14]. The flowchart of the method is illustrated in Fig. 5.

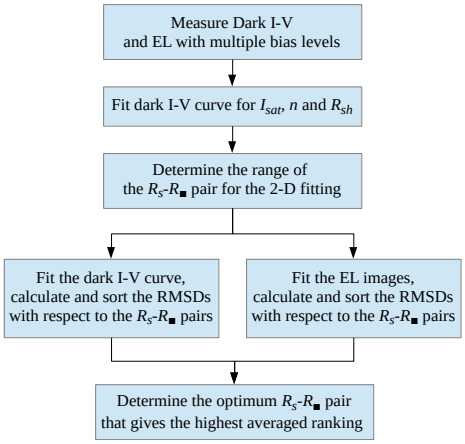

Fig. 5. Flowchart shows the new method for extracting the parameters for the full 2-D SRM.

Eqn. (2) and (3) show the hybrid fitting algorithm and the correlation between the local junction voltage and the EL intensity.

$$\left[\exp\left[\frac{q(\boldsymbol{V}-\boldsymbol{I}R_s)}{nkT}\right]-1 \quad \boldsymbol{V}-\boldsymbol{I}R_s\right]\begin{bmatrix} I_{sat} \\ 1/R_{sh}\end{bmatrix}=[\boldsymbol{I}] \qquad (2)$$

$$\Phi(\boldsymbol{r})=C\exp\left[\frac{qV_j(\boldsymbol{r})}{n(\boldsymbol{r})kT}\right] \qquad (3)$$

Here, n and R_s are in a nonlinear space and are subject to changes through an iterative simplex algorithm. C is a calibration constant.

The sample used for validation is a thin-film a-Si module consisting of 9 cells connected in series. The EL measurements are taken at bias levels I_{SC}, $0.6I_{SC}$ and $0.2I_{SC}$ respectively. The dark I-V of a cell is obtained by dividing the operating voltages the module by 9 while the corresponding operating current values remain unchanged. The size of a single cell is $5.2\times0.5\text{cm}^2$. A 208×20 meshing grid is configured for the 2-D fitting. The resolution of the original EL images is reduced down to 208×20 by dividing each image into 5×5 pixel blocks and calculating the average.

The extracted parameters using the proposed method are listed in Table 1. The dark I-V curve and the line-scan EL profiles generated by the optimum parameter set are highlighted in Fig. 6, and are compared with the original experiment data. The jitters are most likely due to the read out noise of the camera involved rather than the defects. The comparison demonstrates excellent agreement between the reconstructed cell behavior and the measurement results.

Table 1.
Extracted electrical parameters of the a-Si module

J_{sat} (A/cm^2)	3.35×10^{-9}	Hybrid fitting
n	3.82	
Γ_{sh} (Ω.cm^2)	684.96	
Γ_s^i (Ω.cm^2)	2.0	2-D fitting
$R_\blacksquare$ ($\Omega/\square$)	15.0	

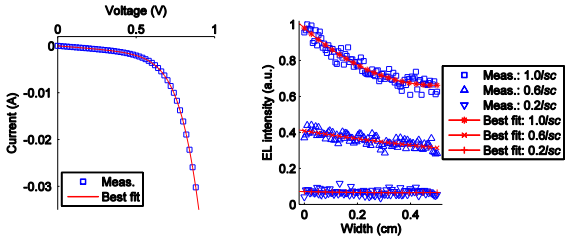

(a) (b)

Fig. 6. Fitting results show the excellent agreement between the simulated (a) dark I-V curve; (b) EL profiles and the measurements.

5. Conclusions

The lateral resistances can cause lateral voltage drops in the cell as well as the corresponding changes of the local current. The use of effective series resistances can cause misinterpretations of the behaviour of PV devices. The proposed fitting method can, for the first time, provide a full parameter set of 2-D models for thin-film PV devices.

Acknowledgements

This work is supported by the project “Stability and Performance of Photovoltaics” funded by RCUK (EP/H040331/1) and by Department of Science and Technology in India.

References

[1] J. Carstensen *et al*., PVSAT-16, pp. 1627-1630.
[2] T. Fuyuki *et al*., *Applied Physics Letters,* vol. 86, 262108, 2005.
[3] T. Trupke *et al*. *Applied Physics Letters,* vol. 87, 093503, 2005.
[4] O. Breitenstein *et al*., *Prog. Photovolt: Res. Appl.,* vol. 11, pp. 515-526, 2003.
[5] D. Hinken *et al*. *Applied Physics Letters,* vol. 97, 182104, 2007.
[6] H. Kampwerth *et al*., *Applied Physics Letters,* vol. 93, 202102, 2008.
[7] O. Breitenstein *et al*., *Phys. Status Solidi RRL,* vol. 4, pp. 7-9, 2010.
[8] C. Shen *et al*., *Solar Energy Materials & Solar Cells,* vol. 109, pp. 77-81, 2013.
[9] P. Vorasayan *et al*., *Solar Energy Materials & Solar Cells,* vol. 95, pp. 111-114, 2011.
[10] X. Wu *et al*., *IET Renewable Power Generation,* vol. 8, pp. 459-466, 2014.
[11] C. Monokroussos *et al*., EU-PVSEC19, pp. 1489-1492.
[12] R. Gottschalg *et al*., *Meas Sci Technol,* vol. 10, pp. 796-804, 1999.
[13] J. Bird, *Engineering Mathematics.* Routledge, 2010.
[14] R. Gottschalg *et al*., *International Journal of Ambient Energy,* vol. 19, pp. 135-142, 1998.